

Analysis of Gas Storage and Transport in Shale using Pressure Pulse Decay Measurements with He, Kr and CO₂

Ye Lyu¹, Youssef Elkady², Anthony R. Kovscek² and Kristian Jessen¹

¹ Mork Family Department of Chemical Engineering and Materials Science, University of Southern California, Los Angeles, California 90089, United States

² Department of Energy Science & Engineering, Stanford University, Stanford, California 94305, United States

Abstract

To predict the recovery of natural gas resources or to estimate the carbon sequestration potential in shales accurately, it is critical to represent the relevant transport and storage mechanisms, that include viscous flow, slip flow, transition flow, Knudsen diffusion, and sorption in multi-porosity (fracture/matrix) systems. Several efforts have been published in the literature aiming to improve our knowledge of how fluids are transported and stored in shale, however, a comprehensive evaluation of shale samples continues to pose a significant challenge.

In this work, we investigate gas transport and sorption in shale using inert (helium -He) and adsorbing (krypton - Kr and carbon dioxide - CO₂) gases by performing pressure pulse-decay measurements on an Eagle Ford shale core sample. Pressure pulse-decay measurements with He (nonsorbing gas) are used to assess the overall porosity. The overall porosity of the sample consists of natural fractures, microcracks, mesopores, and micropores. We present a modified analytical approach for evaluating the mass transfer rate in microcracks and mesopores. A previously established triple-porosity model (TPM) is then utilized to estimate the remaining parameters: the effective gas permeability in the fracture, the mass transfer rates in micropores, and the volume split between mesopores and micropores, by matching the pressure decay data of two He pulse experiments.

Based on the model parameters obtained, the pressure decay behavior of a 3rd He pulse experiment (at higher pressure) is accurately predicted. For adsorbing gases (Kr and CO₂), excess adsorption isotherms at varying bulk pressures, were evaluated by comparing the equilibrium pressure at each pressure stage to the pore volume estimated from He. The adsorption isotherms were then utilized in the TPM to predict gas transport and storage for Kr and CO₂: The gas transport behaviors and storage were predicted with transport coefficients translated from the He. Predictions for Kr and CO₂ are demonstrated to be in excellent agreement with experimental observations, indicating that the modified analytical approach can effectively characterize mass transfer in shales and provide direct input to a TPM representation of the shale core. We furthermore demonstrate and discuss the

importance of the density model for the adsorbed phase in the interpretation of transport and storage. A key contribution of the presented workflow is the demonstration that a TPM approach is effective for interpretation and prediction of gas transport/storage during pressure pulse-decay measurements on shale cores without a need to discretize the shale matrix.

Keywords: Shale Gas, Pressure Pulse-Decay, Diffusion, Sorption, Triple-Porosity Systems, Carbon Storage

1. Introduction

The contribution of natural gas to the United States energy supply is expected to grow over the next three decades and reduce the need for liquid petroleum fuel (EIA, 2021). According to projections, unconventional resources, such as tight or shale gas, will account for almost 90% of the natural gas production. Natural gas is stored in large quantities in shale as free phase and adsorbed phase, with horizontal drilling and multi-stage hydraulic fracturing facilitating the extraction. Induced fractures provide high conductivity channels in shales, that are characterized by very limited matrix permeability in general. The ultra-low permeability and low porosity of the shale matrix, as well as multiphase mobility reductions, clay swelling, and sluggish matrix-fracture exchange, all contribute to a modest recovery of gas in place (Li et al., 2018; Sinal and Lancaster, 1987; Gupta 2009; Wu and Sharma, 2017). Gas transport and storage mechanisms in fractures and matrix must be fully understood to assess accurately and forecast gas recovery from shales. One goal of this effort is to evaluate efficiently laboratory-scale studies on Eagle Ford shale in terms of transport and sorption for inert and adsorbing gases.

Natural (micro) fractures are common in shales, in addition to the fractures induced during well-stimulation. Free gas is extracted initially from fracture networks and macropores (natural or induced) during shale gas production, followed by free gas in mesopores and adsorbed gas in meso/micropores. Adsorbed gas is continuously discharged during shale gas extraction to supplement free gas and extend the production life of shale gas formations. In shale formations, gas transport processes include viscous flow, slip flow, transition flow, and Knudsen diffusion in the bulk phase (Javadpour, 2009; Alnoaimi and Kovscek, 2019; Chen et al., 2019; Lyu et al., 2022), which are tightly coupled with the adsorbed phase (Javadpour, 2009; Akkutlu et al., 2018; Lyu et al., 2021).

Experiments and modeling work for shale samples from various formations have been presented in recent years. Ghanizadeh et al. (2014) conducted experimental measurements to study the fluid permeability (helium, argon, methane, and water) in shale samples from the Scandinavian Alum Shale. Elkady and Kovscek (2020a) utilized Computed Tomography (CT), pulse decay techniques, Scanning Electron Microscopy (SEM), and micro-CT to investigate the effects of CO₂ on fluid transport in Utica and Eagle Ford shale.

Javadpour (2009) introduced a formulation, via Maxwell's theory for a single nanotube, that accounts for the deviations between shale-gas transport and gas transport in conventional formations, i.e., slip flow and Knudsen diffusion. Civan (2010), following the work of Beskok and Karniadakis (1999), developed a model describing gas transport in tight porous media. Freeman et al. (2011) applied the dusty-gas model (DGM) in the TOUGH+ simulator to investigate gas transport in micro- and nano-scale pores. However, the basic transport mechanisms of the gas are still debated due to an incomplete understanding of the gas storage conditions and complex pore structure within the shale matrix. Meanwhile, numerous studies of sorption behavior of tight powdered materials (e.g., Lu et al., 1992; Chalmers et al., 2008) have been presented. However, adsorption/desorption tests performed on whole cores are, in general, expected to be more representative of the subsurface than powdered materials due to the additional surface area created during grinding (André, 2009).

One of the key petrophysical properties of shale is the apparent permeability, that is often many orders of magnitude smaller than that of conventional rocks. Brace et al. (1968) introduced the use of the pulse decay approach to estimate the permeability of tight rocks: Gas transports through a core sample to a downstream reservoir once the upstream reservoir is pressurized. Permeability can then be estimated based on how fast the pressure decays in conjunction with gas properties and the core dimensions. Compared to the traditional steady-state approach, this strategy significantly reduces the time for lab measurement of permeability in tight formations. Furthermore, the pulse decay approach can be extended to evaluate permeability, porosity, and sorption at the same time (Aljamaan et al., 2017).

Several scholars (Yamada and Jones, 1980; Cui et al., 2009; Amaefule et al., 1986; Dicker and Smits, 1988) have identified flaws in the original approach of Brace et al. (1968), including that estimates of permeability are sensitivity to the time interval used in the analysis. Yamada and Jones (1980) investigated situations where the logarithm of the reduced pressure decline is not always linear with time. The authors ascribe this to the fact that the formulation of Brace et al. (1968) ignores the pore volume of the sample. The authors also infer that the closer the pore volume is to the upstream reference volume, the greater the early time departure from an exponential decline will be. Amaefule et al. (1986) further support the observation that a 'zero-porosity' approximation for determining permeability might result in significant errors. Using an experimental approach, Dicker and Smits (1988) were able to resolve this problem when the upstream and downstream reservoir volumes are equal, and the pore volume of the sample is somewhat smaller than both reservoirs. The authors demonstrate that this allows for accurate (within 0.3 percent) interpretations in situations where a simple analytical approximation (Eqns. 1-3) is still accurate.

After initiating a pressure pulse through a core sample, the upstream pressure decays exponentially with time (Dicker and Smits, 1988):

$$P_1 - P_2 = \Delta P \cdot e^{-\alpha t} \quad , \quad (1)$$

$$\ln\left(\frac{P_1 - P_2}{\Delta P}\right) = \ln(p_D) = -\alpha t \quad , \quad (2)$$

where P_1 is the pressure in the upstream reservoir with volume V_1 , P_2 is the downstream pressure, ΔP is the initial pressure difference, V_2 is the downstream volume, p_D is the dimensionless pressure difference between P_1 and P_2 (scaled with ΔP), and α is the exponential decay factor. The effective permeability k of the core then can be estimated from α :

$$\alpha = \frac{kA}{\mu c_g L} \left(\frac{1}{V_1} + \frac{1}{V_2} \right) \quad , \quad (3)$$

where μ is the gas viscosity, c_g is the isothermal gas compressibility, L is the length of the sample, and A is the cross-sectional area of the sample.

The influence of fractures on the permeability evaluation in unconventional samples is one of the most difficult challenges in the industry (Peng et al. 2019). As a result, to develop a technique for permeability measurement in unconventional reservoir rocks, it is necessary to be able to quantify and identify the contributions from cracks and from the matrix. In the analytical approach, the time interval utilized for determining α has a significant impact on the inferred permeability. Normally, the time interval included in the analysis starts a few minutes after the upstream valve is opened to remove the potential impact of adiabatic temperature fluctuations caused by the abrupt change in the upstream pressure (Brace et al., 1968), but also to diminish the impact of fractures on gas transport in the matrix: Peng et al. (2019) suggests that the matrix permeability can be determined by using the pressure-decay data collected during later times.

In recent studies (Lyu et al., 2021; Lyu et al., 2022), we have used helium (He), argon (Ar), and methane (CH₄) to characterize two shale samples from the same depth of the Marcellus formation at different length scales. Using a triple-porosity model (TPM) with transfer functions (based on Vermeulen, 1953 and Zimmerman et al. 1993), we have demonstrated that mass transfer in fractured shales can be characterized by transition flow in the free phase (combination of viscous flow and Knudsen diffusion) and sorption kinetics in the adsorbed phase at high pressures. Apart from an artificial fracture included in the previous work, natural fractures or cracks are also important as higher permeable flow paths during shale gas production and gas storage processes.

In this work, we investigate the mass transfer and sorption behaviors in an Eagle Ford shale core that contains natural fractures. Using a modified analytical approach, the mass transfer rate in the mesopores is estimated via pressure decay experiments with He. The TPM is then used to estimate the remaining parameters including the effective gas permeability of the fracture system, the mass transfer rate in the micropores, and the volume ratio of the meso- and micro-pores in the matrix, by matching the pulse pressure decay data of He. For adsorbing gases (Kr and CO₂ are used in this work), excess adsorption isotherms at varying bulk pressures are calculated by comparing the equilibrium pressure at each pulse experiment to the pore volume estimated by He. The adsorption isotherms are then utilized in the TPM to predict gas transport and storage for Kr and CO₂ with gas transport parameters translated from the He experiments.

To the best of our knowledge, this is the first time that the characteristic time for mass transfer (reciprocal of the mass transfer rate), in the shale matrix, is obtained from a modified analytical method using the pressure-pulse decay technique, and then seamlessly implemented into the mass transfer functions to interpret and predict measurements using a TPM. As the experimental pressures in this study are limited to a relatively low range (up to 30 atm), sorption isotherms were used directly in the modeling for sorbing gases (Kr and CO₂).

2. Methodology

2.1. Experimental approach - Pressure-pulse decay measurements

Pressure pulse decay measurements were conducted on a shale core from the Eagle Ford (Fig. 1). The relevant parameters for the core are summarized in Table 1.

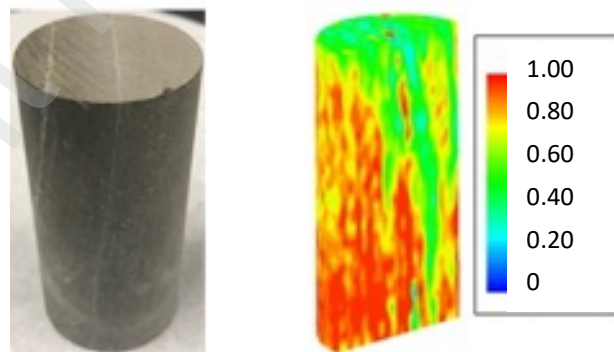


Fig. 1: Eagle Ford shale sample (left) and a reconstructed 3D CT image of the in-situ Kr mass fraction after roughly 2 PV of nitrogen injection (right) (Elkady, 2020). Injection from the top.

Two calcite-filled fractures are visible on the core (see Fig. 1 left) but do not appear to contribute to gas flow. However, a CT image (Fig. 1 right), from a N_2/Kr displacement experiment, indicates the existence of highly permeable pathways (Elkady, 2020). The process for drying and sleeving the core is described in the paper by Elkady and Kovsky (2020b).

Table 1: Eagle Ford shale core dimensions and properties (Elkady and Kovsky, 2020b)

Core	Value
Length (cm)	4.24
Diameter (cm)	2.54
Volume (cm ³)	20.7
Dry Weight (g)	49.8
Bulk Density (g/cm ³)	2.41
Cored Depth (ft)	11,184

The pulse decay setup depicted in **Fig. 2** was used to investigate the rock sample. The upstream reservoir (V_1) is charged by opening Valve 1 to a He supply, while keeping Valve 2 closed after the core has been sleeved and evacuated (Valve 3 is kept open while Valve 4 is closed after evacuation).

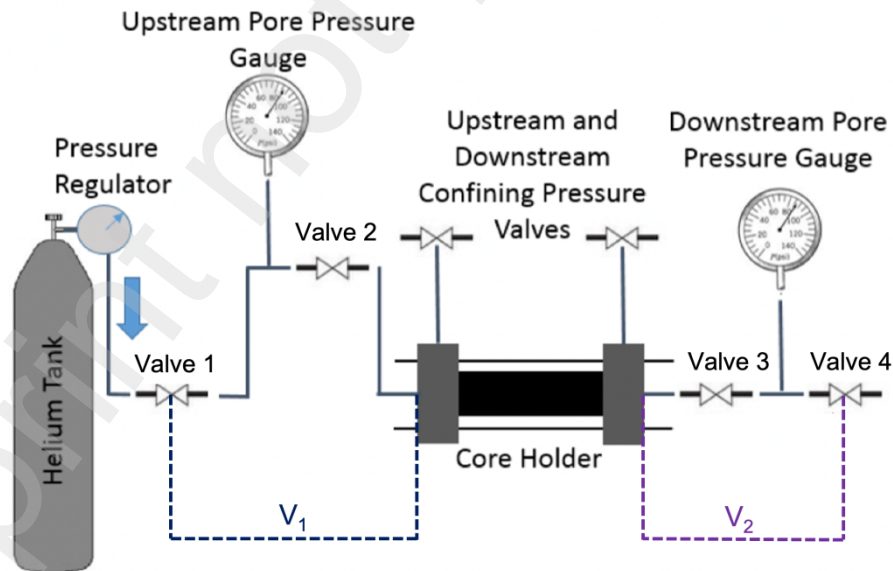


Fig. 2: Pressure-pulse decay experimental set up for measuring mass transfer and sorption in the shale core (Modified from Elkady et al., 2020).

Valve 1 is then closed, and the upstream pressure is monitored until it stabilizes. Valve 2 is then opened, allowing the He to transport through the core. Precalibrated pressure transducers rated for 2000 psia (138 bar) were used to record the pressures upstream and downstream of the system. An experiment concludes as the system pressure stabilizes at the final (equilibrium) level where the upstream and downstream pressures are equal and have not changed for 6 to 12 hours. Fig. 2 also shows the upstream and downstream volumes (V_1 and V_2) used in the interpretation of the pulse decay experiments. An initial recording period of a few seconds was disregarded in the analysis to prevent the impact of adiabatic temperature variations caused by the abrupt change in upstream pressure (Brace et al., 1968). During this brief period, it is assumed that gas expands rapidly from the upstream to the upstream surface of the core.

Petrophysical properties of shale samples can be stress sensitive, largely due to natural fractures and micro-cracks (Heller et al., 2014; Wasaki and Akkutlu, 2015). Thus, in this work, a constant net stress condition was applied. The confining pressure was initially set to 500 psia (34 bar) above the average of the upstream and downstream reservoir pressures. The confining pressure was subsequently adjusted throughout a pulse decay experiment to maintain a net stress of 500 psia (34 bar). In subsequent pulse experiments, additional gas was charged to the upstream reservoir (V_1), while keeping the equilibrium pressure from the previous test in the remainder of the system (core + V_2).

Elkady and Kovscek (2020b) demonstrated that the effective or interconnected porosity of the sample can be calculated from He experiments, using the real gas law (with z-factors from NIST) and a material balance. When determining sample storativity for other gases, He is utilized as a non-sorbing reference gas. Sorbing gases, including Kr and CO₂, adsorb to the mineral surfaces and the organic content (e.g., kerogen) of the sample at varying magnitudes, resulting in excess storage compared to that of He (Nuttall et al., 2005; Vega et al., 2014; Aljamaan et al., 2017b; Elkady and Kovscek, 2020b). The excess sorption can be calculated from

$$n_{ex} = n_{total} - C_{eq}V_{He} \quad , \quad (4)$$

where n_{ex} (mol) is the excess adsorption, n_{total} (mol) is the amount of gas (free and sorbed) in the sample at the end of a given pulse experiment, C_{eq} (mol/cm³) is the gas concentration at the equilibrium, and V_{He} (cm³) is the average pore volume (free gas volume) calculated from the He pressure pulse measurements. The absolute adsorption for Kr and CO₂ can then be calculated as:

$$n_{abs} = \frac{n_{ex}}{1 - \rho_{ads}/\rho_{gas}} \quad . \quad (5)$$

n_{abs} (mol) is the absolute adsorption, ρ_{ads} (mol/ cm³) is molar density of the adsorbed phase, and ρ_{gas} (mol/cm³) is the density of the free gas phase (available from the NIST database - Lemmon et al., 2005). Absolute adsorption accounts for the adsorbed phase volume in the pore space (Lin and Kavscek, 2014), that can become significant as the pore pressure increases. Excess gas moles are utilized to determine the actual (absolute) adsorbed gas moles using the molar density ratio of the two phases since absolute adsorption cannot be measured directly in the lab. We note that the density of the adsorbed phase is likely to have a considerable influence on the gas storage estimation in shale (Lyu et al., 2022).

2.2. Modeling approach

2.2.1. Triple-porosity model

In this work, we modify the TPM, presented in detail in our prior work on shale characterization using He and Ar (Lyu et al., 2021), to analyze gas transport and storage. The overall pore volume, V_t (cm³), of the shale core is divided into the volume of natural fractures, V_f (cm³), and the overall pore volume of the shale matrix, V_p (cm³). Natural fractures present in the shale core serve as flow pathways connecting the upstream reservoir and the downstream reservoir. Although these fractures may have unknown geometries and tortuosity, we integrate and represent them as an effective fracture system, as shown in **Fig. 3**.

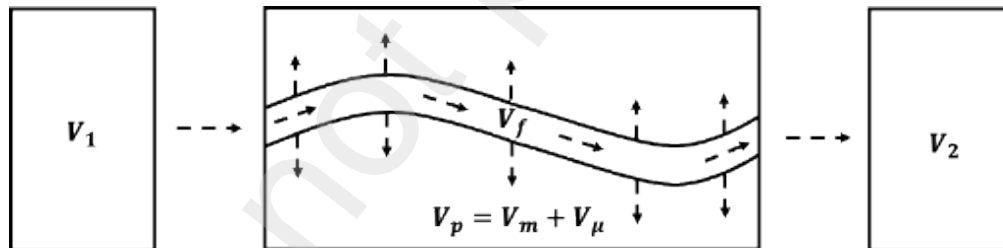


Fig. 3: Conceptual model for shale core pressure-pulse decay experiments.

The total matrix pore volume V_p includes a mesopore volume, V_m (cm³), consisting of mesopores and any microcracks in the shale matrix, and the micropore volume V_μ (cm³). We assume that the effective fracture controls/dominates transport between the up- and down-stream reservoir volumes, V_1 and V_2 .

The formulation of the TPM (Lyu et al., 2021), considers the fracture system as a 1D object that can communicate with the matrix in a hierarchical fashion. The mass exchange rates between the effective fracture system and the mesopores, as well as the mass exchange rates between the mesopores and micropores (Eqns. 9-10), are described by

transfer functions (following the work of Vermeulen, 1953 and Zimmerman et al., 1993) after volume-averaging the matrix under the assumption that gas must transport from the effective fracture to the mesopores before reaching the micropores:

$$\text{Fracture system:} \quad \frac{\partial V_f C_f}{\partial t} + \frac{\partial N_{s,f}}{\partial t} + V_f \nabla F_f = -V_m \Gamma_m \quad , \quad (6)$$

$$\text{Mesoporous matrix:} \quad \frac{\partial V_m C_m}{\partial t} + \frac{\partial N_{s,m}}{\partial t} = V_m \Gamma_m - V_\mu \Gamma_\mu \quad , \quad (7)$$

$$\text{Microporous matrix:} \quad \frac{\partial V_\mu C_\mu}{\partial t} + \frac{\partial N_{s,\mu}}{\partial t} = V_\mu \Gamma_\mu \quad , \quad (8)$$

$$\Gamma_m = \sigma_m D_m (C_f - C_m) \beta_m \quad , \quad (9)$$

$$\Gamma_\mu = \sigma_\mu D_\mu (C_m - C_\mu) \beta_\mu \quad . \quad (10)$$

Here, C_f , C_m and C_μ (mol/cm³) are the molar concentrations of free gas in the fracture, mesopores and micropores, respectively. F_f (mol/cm²/s) is the gas flux in the fracture system. Γ_m (mol/cm³/s) is the transfer rate between the fracture and shale matrix (mesopores) and Γ_μ (mol/cm³/s) is the transfer rate between the mesopores and the micropores. $N_{s,f}$, $N_{s,m}$ and $N_{s,\mu}$ (mol) are the adsorbed amounts in the fracture, mesopores and micropores, respectively. Both transfer functions Γ_j ($j = m, \mu$) include the product of the shape factor σ_j , and the effective diffusivity D_j . β_j is a dimensionless function of initial and boundary conditions that accounts for time dependent gradients inside the meso/microporous segments (Vermeulen, 1953; Zimmerman et al., 1993; Lim and Aziz, 1995; Zhang et al, 2022).

Gas transport in the effective fracture system is defined by an effective group of parameters that includes apparent permeability k_f (cm²), cross-sectional area A_f (cm²), and characteristic length L_f (cm): The flux F_f (mol/cm²/s) in the fracture system is then calculated from

$$F_f = -\frac{\partial}{\partial x_f} \left(C_f \frac{k_f}{\mu_f} \frac{\partial p_f}{\partial x_f} \right) \quad . \quad (11)$$

The gas flow in the effective fracture system may include contributions from Darcy flow (viscous flow) and slip on the fracture wall(s), and therefore, k_f is represented by the Dusty-Gas-Model (DGM, see Lyu et al., 2022)

$$k_f = B + \frac{D_k \mu_f}{p_f} \left(1 - \frac{p_f}{Z} \frac{dZ}{dp_f} \right) \quad . \quad (12)$$

C_f (mol/cm³), μ_f (psia·s), and p_f (psia), denote the gas concentration, viscosity, and pressure in the fracture, B (cm²) is the viscous flow parameter, D_k (cm²/s) is the Knudsen diffusivity, and Z is the gas compressibility factor. We note that V_f defines the effective cross-sectional area of the fracture system $A_f = V_f/L_f$. In this work, the V_f represents a small fraction of the overall porosity of the shale core only. An initial sensitivity test of the fracture volume on the modeling results was performed (Appendix A). It is observed that, with other parameters fixed, the fracture volume has a marginal impact on the pressure decay behavior when $V_f < 10\%$ the total pore volume. To reduce the modeling complexity, we therefore assign the volume of the effective fracture system to 1% of the core porosity, to arrive at two parameters (BA_f/L_f and $D_k A_f/L_f$) controlling the gas transport in the fracture system.

For the shale matrix, the inverse of the characteristic time (mass transfer rate), is represented by the product of a shape factor σ_j (cm⁻²) and the effective diffusivity D_j (cm²/s), where $j = m, \mu$ denote the mesoporous and microporous segments, respectively. The product, $\sigma_j D_j$, includes the tortuosity of the matrix segments. The porosity and tortuosity of the core, and the shape factor σ_j are assumed to remain constant because the net stress was kept constant throughout the experiments. The mass transfer rates can be estimated directly from the pressure decay data of He using a modified analytical approach (see details below) and then translated to higher pressures and/or other gases. This requires knowledge of how the effective diffusivity varies with pressure for different gases.

Because slip- and transition-flow are expected to dominate gas transport in mesopores, as demonstrated in Appendix B based on relevant Knudsen numbers (Schaaf and Chambre, 1961; Roy et al., 2003), the effective diffusivity in the mesopores can be represented by the Dusty gas model (Mason and Malinauskas, 1983; Ho and Webb, 2006; Sakhaee-Pour and Bryant, 2012). This model combines viscous flow and Knudsen diffusion and the molar flux, F_m (mol/cm²/s), can be reformulated as a diffusion-type equation with an effective diffusivity, D_m that depends on pressure

$$F_m = -C \frac{B}{\mu} \nabla p - D_k \nabla C = - \left[\frac{pB}{\mu} \left(1 + \frac{C}{Z} \frac{dZ}{dC} \right) + D_k \right] \nabla C = -D_m \nabla C_m \quad . \quad (13)$$

Another popular model developed by Beskok and Karniadakis (1999) and modified by Civan (2010) can also be utilized to describe the apparent permeability in tight porous media. However, the explicit expression of the gas transport coefficient in the shale matrix

was not the objective of this work. Instead, only the correlations of coefficients among different gases and pressures were investigated in this work. The two models work similarly for this purpose, as demonstrated in Lyu et al. (2022) and in Appendix C.

In the microporous region, where pore dimensions are comparable to the size of the molecules, Knudsen diffusion is expected to dominate the gas transport. Thus, the effective diffusivity in micropores is considered to be independent of pressure and rescaled based on the molecular weight of relevant gases. The molar flux of gas in the shale matrix can then be expressed as

$$F_j = -D_j \nabla C_j, \quad j = m, \mu \quad (14)$$

Because the fractures in the core are more permeable than the shale matrix and only account for a very small volume, relative to the upstream and downstream reservoirs as well as the pore volume in the matrix, the pressure-decay at later times is mainly controlled by the matrix. Accordingly, the matrix permeability can be determined using the pressure-decay data collected during the later times (Peng et al., 2019). The analytical approach of Dicker and Smits (1988) (see Eqn. 3), can be re-written as

$$\alpha_m = \left(\frac{k \cdot V/L}{\mu c_g L} \right)_m \left(\frac{1}{V_1} + \frac{1}{V_2} \right) = \sigma_m D_m \left(\frac{V_m}{V_1} + \frac{V_m}{V_2} \right) \quad , \quad (15)$$

$$D_m = \left(\frac{k}{\mu c_g} \right)_m, \quad \sigma_m = \frac{1}{L_m^2} \quad . \quad (16)$$

The slope, α_m , for transport in the mesopores as obtained from the plot of $\ln(P_D)$ versus time now represents the product of the shape factor σ_m , the effective diffusivity D_m , and a volume factor $(V_m/V_1 + V_m/V_2)$. Thus, the characteristic mass transfer rate in mesopores ($\sigma_m D_m$) (1/s) can be estimated directly from pressure decay data using this modified method.

Ideally, a similar approach could be used to estimate the characteristic time for transport in the microporous regions of the matrix. However, initial tests demonstrated that the approach is highly sensitive to data accuracy when the pressure difference becomes comparable to the accuracy of the pressure transducers. Accordingly, the characteristic time for mass transfer in the micropores is estimated from the pulse decay data with He as detailed further below.

2.2.2. Sorption in the matrix

The Langmuir adsorption isotherm is used to interpret the absolute adsorption for Kr, and the isotherm is applied directly in the analysis of the pressure decay experiments. This assumes that the characteristic time for adsorption is small, and that sorption kinetics can be ignored

$$C_s = C_{s,max} \cdot \theta, \quad \theta = \frac{Kp}{1 + Kp} \quad (17)$$

Here, C_s (mol/kg) is the absolute sorption that depends on the maximum monolayer adsorption capacity of the shale $C_{s,max}$ (mol/kg) and the surface coverage θ . θ can be computed from the equilibrium constant K (psia⁻¹) and the bulk phase pressure p (psia).

While the Langmuir isotherms is suitable for modeling monolayer (θ less than one) sorption (e.g. N₂, CH₄ and Kr at low pressure or high temperature), the BET adsorption model, developed by Brunauer et al. (1938), is used for multilayer sorption (θ can be greater than one) of CO₂ at high pressure, that is known to have a stronger affinity to shales than e.g. CH₄. The BET model can be written as

$$C_s = C_{s,max} \cdot \theta = C_{s,max} \frac{c \left(\frac{p}{p_o} \right) \left[1 - (n+1) \left(\frac{p}{p_o} \right)^n + n \left(\frac{p}{p_o} \right)^{n+1} \right]}{\left(1 - \frac{p}{p_o} \right) \left[1 + (c-1) \left(\frac{p}{p_o} \right) - c \left(\frac{p}{p_o} \right)^{n+1} \right]} \quad (18)$$

where p_o (psia) is the saturation pressure at the experimental temperature ($p_o = 833$ psia in this work), c is a dimensionless constant, related to the heat of adsorption, and n is the maximum number of adsorbed layers.

To implement the adsorption isotherms in the TPM, the amounts of adsorbed gas can be calculated as

$$N_{s,j} = W \frac{A_j}{c A_t} C_{s,j} \quad (j = f, m, \mu) \quad (19)$$

and the impact on pore volumes due to adsorption can be evaluated from

$$V_j = V_{j,0} - V_{ads,j} = V_{j,0} - N_{s,j} / \rho_{ads,j} \quad (j = f, m, \mu) \quad (20)$$

In Eqns. (19-20), W_c (kg) is the core weight, A_j is the surface area of fracture, mesopores, and micropores per unit mass ($j = f, m, \mu$) and A_t is the total surface area per unit mass. The fraction of the total surface area assigned to the fracture, mesopores, or micropores, A_j/A_t , can be estimated as the ratio between the specific pore volume and the total pore volume, as demonstrated by Lyu et al. (2021). V_j (cm³) is the current pore volume, $V_{j,0}$ (cm³) is the pore volume for He, and $V_{ads,j}$ (cm³) is the adsorbate volume based on the molar density $\rho_{ads,j}$ (mol/cm³) of the adsorbed phase.

3. Results

A total of 8 pulse-decay experiments - 3 with He, 3 with Kr and 2 with CO₂ – were performed as part of this work. In the following sections, we present and interpret the experimental observations towards a detailed characterization of transport and sorption in fractured shale.

3.1. Porosity and adsorption isotherms

Fig. 4 reports the pressure history of the upstream (blue) and downstream (black) reservoirs for a series of three He pulse-decay experiments.

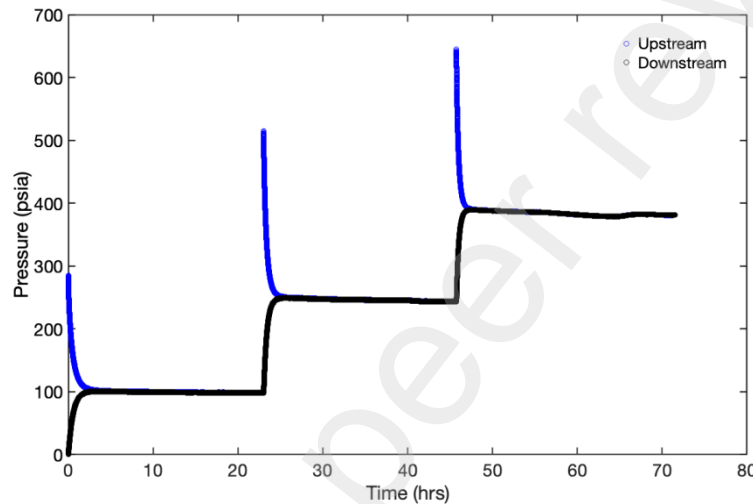


Fig. 4: Pressure-pulse decay experiments with He ($T = 20\text{ }^{\circ}\text{C}$).

Each pulse of He provides an estimate of the pore volume (and porosity) because He is assumed to be nonsorbing. The He porosity value used here is the average of the porosity measurements derived from each pulse. As demonstrated by Elkady and Kavscek (2020b), the average He porosity for this Eagle Ford sample is 9.8% ($V_t = 2.02\text{ cm}^3$), based on the He pressure pulse decay data. This further defines the fracture volume (V_f) to represent 0.02 cm^3 from the assumption of $V_f = V_t/100$ as discussed above.

For sorbing gases (CO₂/Kr), an apparent porosity or storativity can be calculated at the end of each pressure pulse. The storativity in standard cubic feet (scf) of gas per ton of rock ($1\text{ scf/ton} = 1.196 \cdot 10^{-3}\text{ mol/kg}$) at each equilibrium pore pressure was calculated for Kr and CO₂ and are reported in **Fig. 5**. We note that the storativity ($n_{\text{total}}/\text{mass of sample}$ – see Eq. 3) includes contributions from free and adsorbed gas. A comparison of the storativity of CO₂ and Kr (surrogate for CH₄) indicates a clear net storage potential from shale gas operations over the pressure range investigated here.

The excess adsorption can be expressed in terms of absolute adsorption and the density ratio between adsorbed and free gas (see Eqn. 5). When the absolute adsorption is represented by an isotherm model (e.g. Langmuir or BET – see Eqn. 17-18) this allows one to estimate the parameters of the model from the excess data, based on an assumption of the adsorbate phase density. As discussed in the previous interpretation of CH₄ adsorption on a full-diameter Marcellus shale core (Lyu et al., 2022), the selected density model can have a significant impact on the calculated absolute sorption. The density at the normal boiling point was initially selected here because of its popularity and the excellent agreement with the excess sorption data of CH₄ in the previous work. The resultant model parameters for the Langmuir (Kr) and the BET (CO₂) models are reported in **Table 2** while **Fig. 6** (right) reports the calculated absolute adsorption for the two gases.

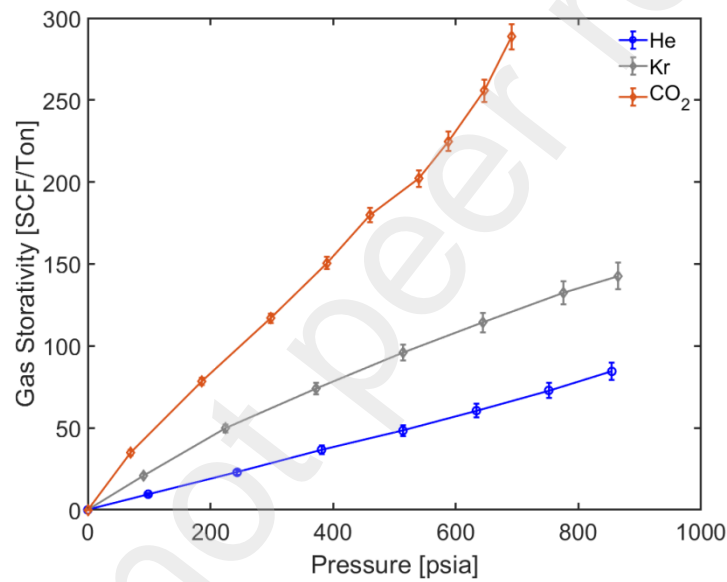


Fig. 5: Gas storativity in the shale sample.

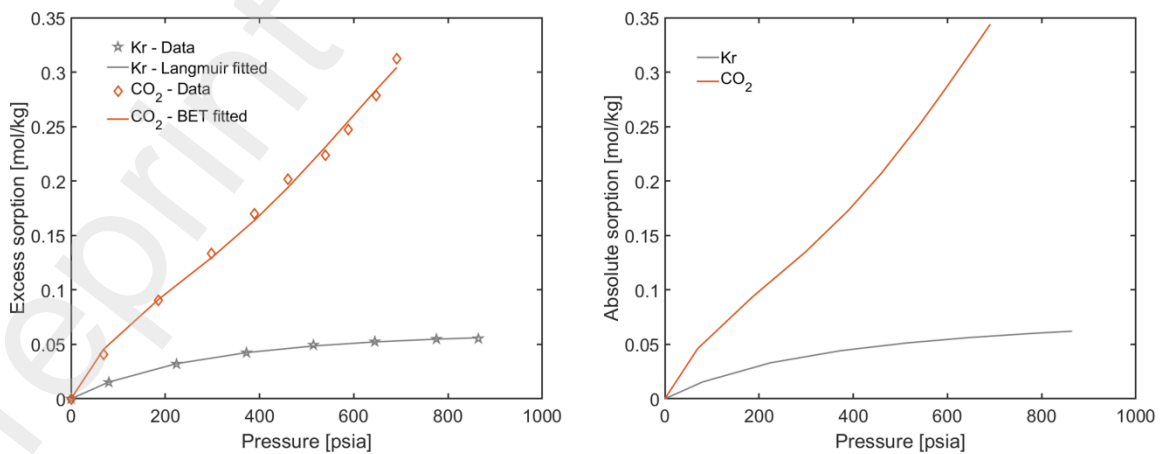


Fig. 6: Excess adsorption (left) and absolute adsorption (right) modeling results.

It should be noted that the adsorption isotherms in this work represent an averaged behavior of the whole sample, therefore, the maximum number of layers (n) in the BET model is not related to a single pore diameter, but rather to the average of the pore-size distribution.

Table 2: Model parameters for Kr and CO₂ adsorption isotherms.

	ρ_{ads} (mol/cm ³)	$C_{s,max}$ (mol/kg)	K (psia ⁻¹)	c (-)	n (-)
Kr	28.80e-3	89.66e-3	2.60e-3		
CO ₂	25.02e-3	109.47e-3		6.88	7

3.2. Mass transfer in matrix

Following the approach of Dickers and Smit (1988), discussed above, we plot two pulses of He data in **Fig. 7**, to obtain two slopes of $\ln\left(\frac{P_1 - P_2}{\Delta P}\right)$ versus t .

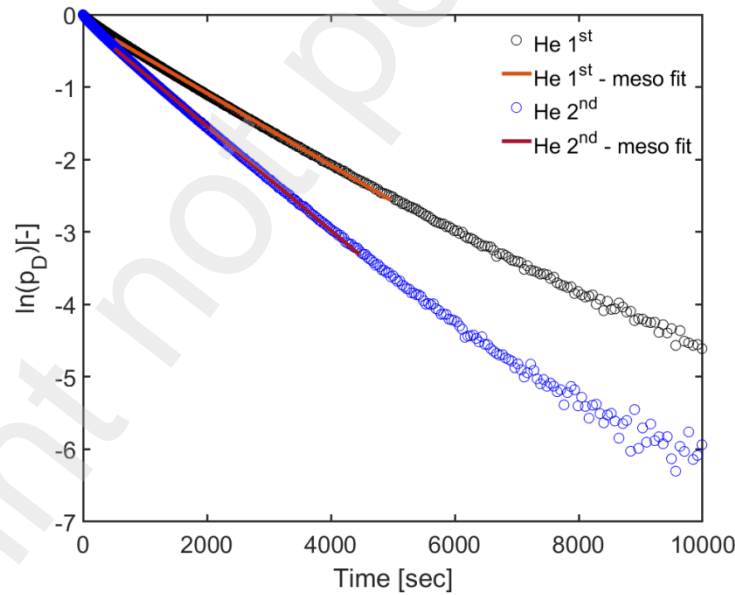


Fig. 7: Mass transfer rate characterization for mesopores using the modified analytical approach with the 1st and 2nd pulses of He pressure decay.

The slopes were utilized to estimate the mass transfer rates for the mesopores of the 1st and 2nd pulses of He, following the modified interpretation outlined in Eqns. 15-16. We note that the mass transfer rate is the inverse of the characteristic time for mass transfer and that

each slope corresponds to a given pressure range. Accordingly, once the volume of the mesopores (or micropores) is known, the mass transfer rates for the mesopores can be estimated from the slopes as

$$(\sigma D)_m = \alpha_m / \left(\frac{V_m}{V_1} + \frac{V_m}{V_2} \right) \quad , \quad (21)$$

with m denoting the mesoporous region. Determination of the mesopore volume is discussed further below.

3.3. Pressure decay interpretation and validation with He

The TPM includes the following parameters: The effective permeability of the fracture system ($k_f A_f / L_f$), that can be expanded into two parameters (BA_f / L_f and $D_k A_f / L_f$), the mass transfer rates in the mesopores and micropores, $\sigma_m D_m$ and $\sigma_\mu D_\mu$, and the pore volume distribution in the shale matrix, V_m / V_p (with $V_p = V_t - V_f$). The workflow for obtaining the relevant model parameters is detailed in Appendix D: The model parameters are first calibrated with two pressure decay experiments using He. Because transport parameters are pressure-dependent (i.e., k_f depends on pressure, see Eqn. 12, and $\sigma_m D_m$ is considered as an average characteristic time over the relevant pressure range in each pulse), matching two pulses simultaneously allows us to delineate the dependency of transport coefficients on gas pressure. After the calibration, a 3rd pulse-decay for He is used to validate the estimated parameters. The remaining undetermined parameters were estimated by matching the 1st and 2nd He pulses simultaneously using a non-linear regression approach. The estimated model parameters, including 95% confidence intervals (CI), are reported in **Table 3**. **Fig. 8** compares modeling and experiments after regression, and we observe a good agreement with RMSE values of less than 0.1% of the pressure ranges.

Table 3: Parameter estimation using the 1st and 2nd pulses of He pressure decay.

	BA_f / L_f (10^{-15} cm ³)	$D_k A_f / L_f$ (10^{-4} cm ³ /s)	$(\sigma D)_\mu$ (10^{-6} 1/s)	V_m / V_p (%)
Results	8.02	5.95	27.31	72.58
95% CI	[8.00,8.04]	[5.94,5.97]	[27.31, 27.31]	[72.49, 72.65]

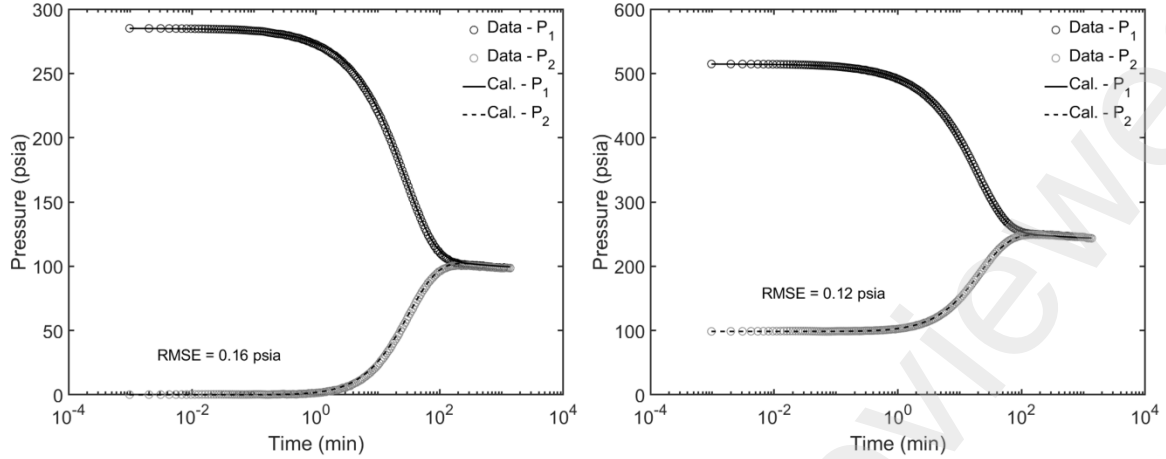


Fig. 8: Comparison of calculation results and data for the 1st and 2nd He pressure decay experiments after parameter estimation.

From the estimated volume split (V_m/V_p) and the slope obtained from the modified analytical approach (Fig. 7), the mass transfer rates in the mesopores are calculated to $(\sigma D)_m = 574.72 \times 10^{-6}$ (1/s) and $(\sigma D)_m = 825.36 \times 10^{-6}$ (1/s) for the 1st and 2nd He decay experiments, respectively.

To predict the behavior of other pressure decay experiments (He, Kr, and CO₂), the transport coefficients must be rescaled to account for variations in pressure and molecular properties. For transport in the fracture, BA_f/L_f only depends on the fracture geometry (fracture aperture etc.), and $D_k A_f/L_f$ depends on the fracture geometry and molecular weight of the gas (see Eqn. 23). Accordingly, the rescaling of fracture transport parameters is straight forward.

The rescaling factor for the mesoporous transport must be estimated from the ratio of effective diffusivities (D_m) at relevant pressure ranges (and component properties). Following the approach of Lyu et al. (2021), we estimate the characteristic time for mass transfer t^* (s)

$$t^* = 1/(\sigma D)_m = L_c^2/D_m \quad , \quad (22)$$

where L_c is the characteristic length and D_m is the effective diffusivity. To evaluate D_m , as a function of pressure and M_w , for scaling-purposes, we consider a single cylindrical pore with an effective radius r_m (cm). The viscous flow parameter and the Knudsen diffusivity are then given as a function of r_m

$$B = \frac{r_m^2}{8}, D_k = \frac{2r_m}{3} \sqrt{\frac{8R_g T}{\pi M_w}}, \quad (23)$$

where M_w (kg/mol) is the molecular weight, R_g (J/mol/K) is the gas constant, and T (K) is the temperature. For a given value of r_m , D_m can now be calculated as a function of pressure for relevant gases via

$$D_m = \frac{pB}{\mu} \left(1 + \frac{C}{z} \frac{dz}{dC}\right) + D_k \quad (24)$$

We assume that the shape factor σ is constant between experiments (at constant net stress), such that the product $(\sigma D)_m$ only depends on D_m . However, unlike our previous work, the average pore size (or pore size distribution) of the shale matrix is not known for the current shale sample. Therefore, an effective pore size must be estimated based on the ratio of characteristic times (or D_m) for the two He experiments reported in Table 3:

$$t_1^*/t_2^* = D_{m,2}/D_{m,1} \quad (25)$$

An average pressure used for evaluating D_m (in Eq. 24) and in the estimation of t^* in Eq. 25 must represent the pulse decay process. Here, we use the average of the maximum pressure in the fracture, $p_{f,max}$, and the minimum pressure in the micropores, $p_{2,ini}$ (initial downstream pressure of each pulse). $p_{f,max}$ can be estimated from a material balance by assuming there is a fast expansion from upstream to downstream.

$$\frac{p_{1,ini}}{Z_{1,ini}} V_1 + \frac{p_{2,ini}}{Z_{2,ini}} (V_2 + V_f) \sim \frac{p_{f,max}}{Z_{f,max}} (V_1 + V_2 + V_f) \quad (26)$$

By combining Eqs. (24-26), with gas properties from NIST, we find an effective pore radius of 84 nm. We note that because the actual geometry of the shale matrix is much more complex than the single pore approximation, the estimated value of the effective equivalent falls beyond the standard pore size range of a mesopore (2–50 nm). This in turn suggests that the characteristic time estimated from the He expansion experiments includes contributions from a range of pores that are not fully aligned with the standard range (the TPM is not familiar with the standard range). Based on the effective pore radius, we can now translate the characteristic time for mass transfer in the mesoporous between pulses of difference pressure and for different gases via Eq. 24.

For the microporous region, we assume that Knudsen diffusivity dominates the gas transport. Accordingly, the scaling factor between gases (not dependent on pressure) is given by the square root of the ratio of molecular weights. Thus, the mass transfer rates, (

$\sigma D)_\mu$, were rescaled from He to Kr and CO₂ by a factor of about 0.22 ($\sqrt{4.0026/83.798}$) and 0.30 ($\sqrt{4.0026/44.009}$), respectively.

The mass transfer rates for the mesopores and micropores at the corresponding experimental pressure ranges were then rescaled and reported in **Table 4** below. To validate the rescaling approach, we predict the 3rd He pulse experiment with parameters from Tables 3+4 and compare calculations with experimental observations in **Fig. 9**. We observe a good agreement between model and experiment with a RMSE of ~0.05% over the relevant pressure range in support of the rescaling approach outlined above.

Table 4: Rescaling of (σD) for prediction of additional pulse-decay experiments.

Pulse	Source	$(\sigma D)_m$ (10^{-6} 1/s)	$(\sigma D)_\mu$ (10^{-6} 1/s)
1 st He	Estimated	574.72	27.31
2 nd He	Estimated	825.36	27.31
3 rd He	Rescaled	1117.80	27.31
1 st Kr	Rescaled	241.24	6.01
2 nd Kr	Rescaled	477.24	6.01
3 rd Kr	Rescaled	733.46	6.01
1 st CO ₂	Rescaled	268.69	8.23
2 nd CO ₂	Rescaled	402.43	8.23

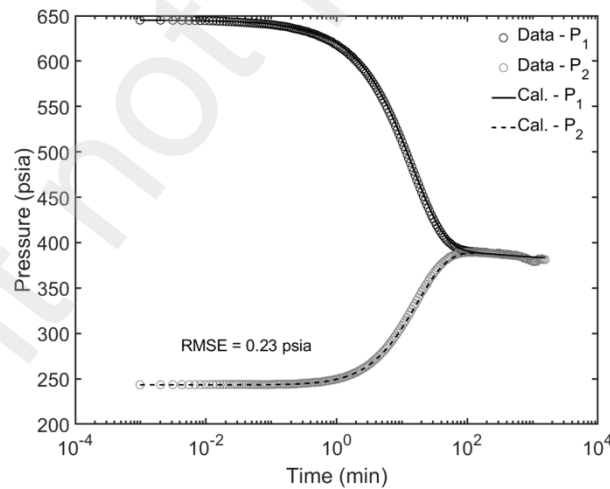


Fig. 9: Model prediction and experimental observations for 3rd He decay experiment.

3.4. Pressure decay predictions for Kr and CO₂

To predict the gas transport and storage for adsorbing gases, i.e., Kr and CO₂, the sorption behaviors were integrated into the TPM. In this work, we represent the adsorption of gases

directly from the sorption isotherms discussed above by assuming equilibrium between free and adsorbed gas. This contrasts with our previous work (Lyu et al., 2022), where sorption kinetics were included in the modeling. For the present sample, we do not have separate measurements of the sorption (including dynamics), and we select to work with isotherms to reduce the number of model parameters that must be estimated from the pulse-decay experiments. The equilibrium assumption is further supported by the lower temperature of these experiments as compared to our previous work (20 °C vs 50 °C).

Adsorption of gases impacts both the storativity and the gas transport due to the link between adsorbed-phase volume, porosity and apparent permeability. The apparent permeability of a fracture depends strongly on the fracture geometry. For a planar geometry, B is proportional to the square of the fracture aperture h_f^2 while D_k is a function of h_f . In this work, we include the impact of adsorbed gas on the fracture permeability, while the porosity reduction in the matrix, due to sorption, is captured via Eqn. 20.

The adsorbed phase volume along the fracture is assumed to contribute uniformly to the porosity reduction (Eqn. 20), providing for a simple representation of the impact on the apparent permeability:

$$B = B_0 \cdot \left(\frac{V_f}{V_{f,0}}\right)^{2\gamma}, D_k = D_{k,0} \cdot \left(\frac{V_f}{V_{f,0}}\right)^\gamma, \quad (27)$$

where B , D_k , and V_f represent the current values, and B_0 , $D_{k,0}$, and $V_{f,0}$ are the reference values obtained from the He experiments (no adsorption). γ depends on the geometry of the fracture, e.g., $\gamma=1$ for planar fractures as assumed in this work.

With adsorption isotherms parameters from Table 2 (and transport properties from Table 4) included in the TPM, the pressure responses from the Kr experiments were initially predicted and are compared to the experimental observations in **Fig. 10**. We observe a good agreement between experiments and model predictions with small RMSE values over the relevant pressure-decay ranges.

For the Kr experiments, we predict that the impact of sorption on the porosity and apparent permeability of the fracture (and matrix) is insignificant and corresponding to a maximum of 4% of the fracture volume (see Appendix E). The selected adsorbate density model for Kr (density at the normal boiling point) appears to work well in part due to the limited amount of adsorption at the relevant conditions (see Figs. 5-6).

Next, we consider the CO₂ pulse decay experiments. For adsorbing gases with high affinity to shale, e.g., CO₂, the pressure decay behavior is more likely to be sensitive to the representation of the adsorbed phase density. The default adsorbate density model used here (density at the normal boiling point) was initially combined with the translated transport properties (Table 7), to predict the two pulse-decay experiments. A comparison on the model predictions with the experimental observations is provided in **Fig. 11**.

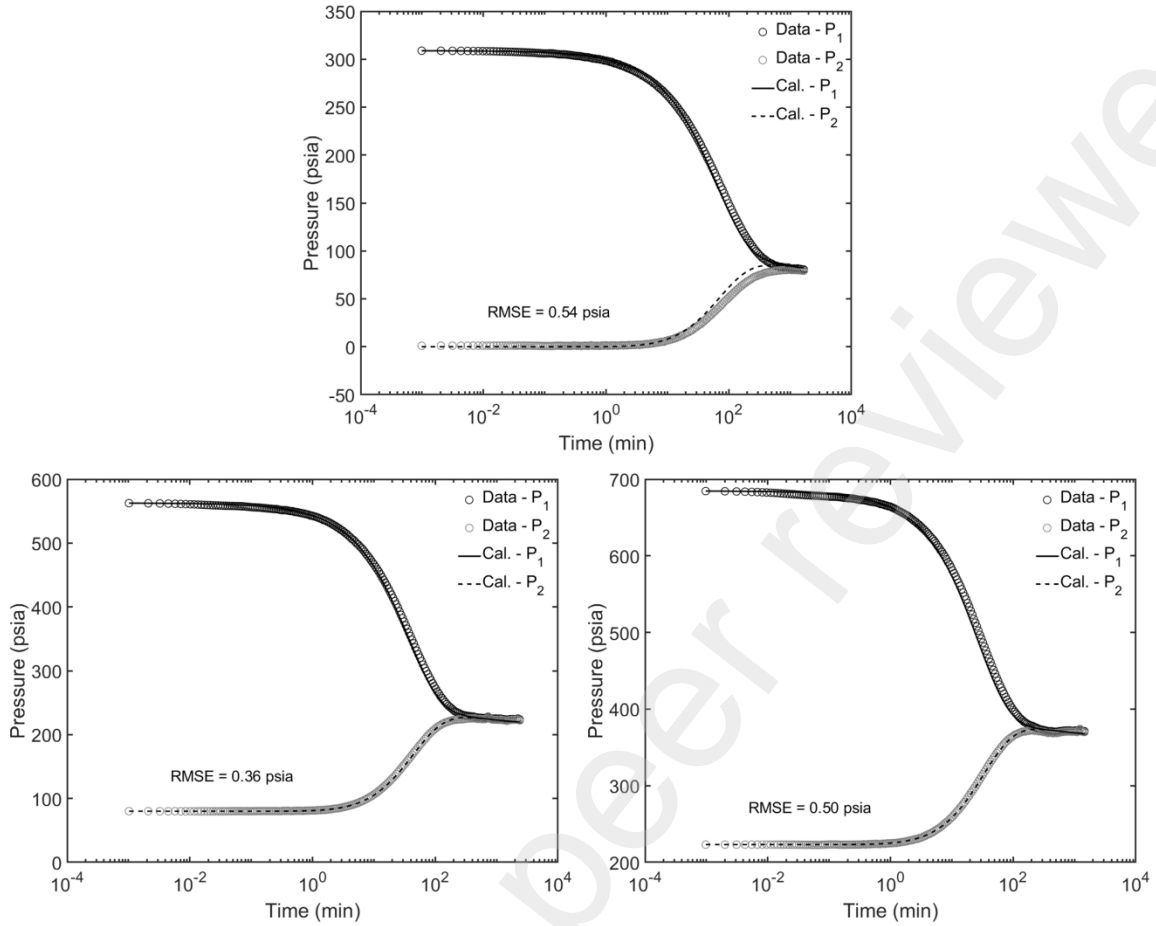


Fig. 10: Comparison of model predictions with experimental observations for the 1st (top), 2nd (left-bottom), and 3rd (right-bottom) Kr experiments.

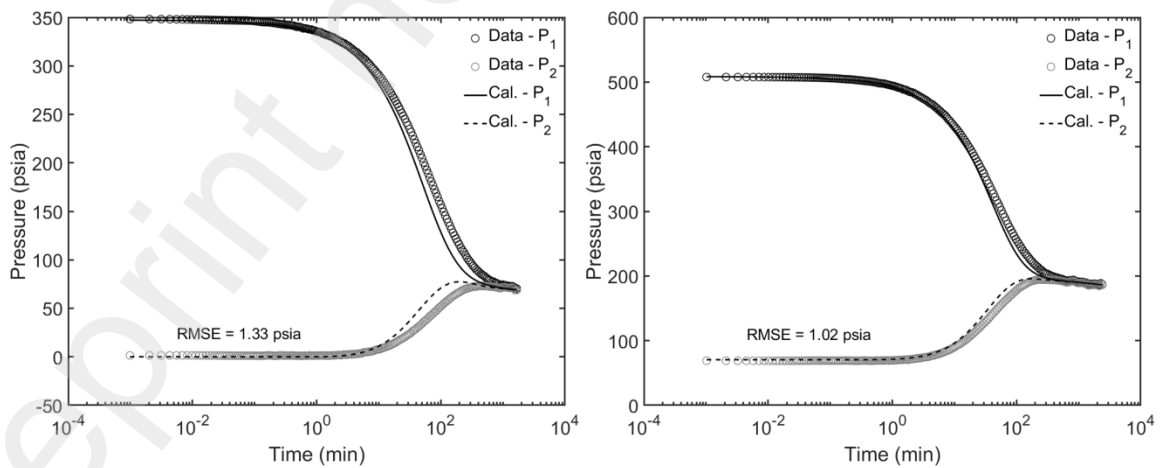


Fig. 11: Comparison of model predictions and experimental data for the 1st (left) and 2nd (right) CO₂ experiments.

We observe that the model response is faster than the experimental observations, suggesting that the transport in the fracture system is overestimated. This, in turn, indicates that a) the selected density model of the adsorbed CO₂ is not adequate in representing the porosity (permeability) reduction in the fracture (the predicted porosity reduction is reported in Appendix E), or that b) swelling of the matrix occurs in tandem with the porosity reduction due to adsorbate volume (Kamali-Asl et al., 2022). If matrix swelling occurs due to adsorption of CO₂ in the matrix, the available data does not allow us to separate this impact from the role of the adsorbate phase density.

At this stage, we explore an empirical adsorbate density model that depends on the surface coverage, θ , during a multilayer adsorption process for CO₂ (see Eqn. 18)

$$\rho_{ads} = M \cdot \theta^{2/3} \quad . \quad (28)$$

This model predicts an increase in the adsorbate density/volume as the fractional coverage increases and Eqns. (19-20) reduce to

$$V_{ads,j} = W \frac{A_j}{c A_t} C_{s,max} \theta^{1/3} / M \quad , \quad j = f, m, \mu \quad . \quad (29)$$

Here, the adsorbate density for a monolayer and full coverage of the adsorbent surface ($\theta = 1$) is given by M (mol/cm³). M is an unknown parameter that was estimated from simultaneous minimization of errors between the model and 1) the excess sorption isotherm; and 2) the 1st pulse-decay experiment with CO₂. An estimated value of $M=12.26 \times 10^{-3}$ mol/cm³ provides for the best agreement (see **Fig. 12** – left and Appendix E).

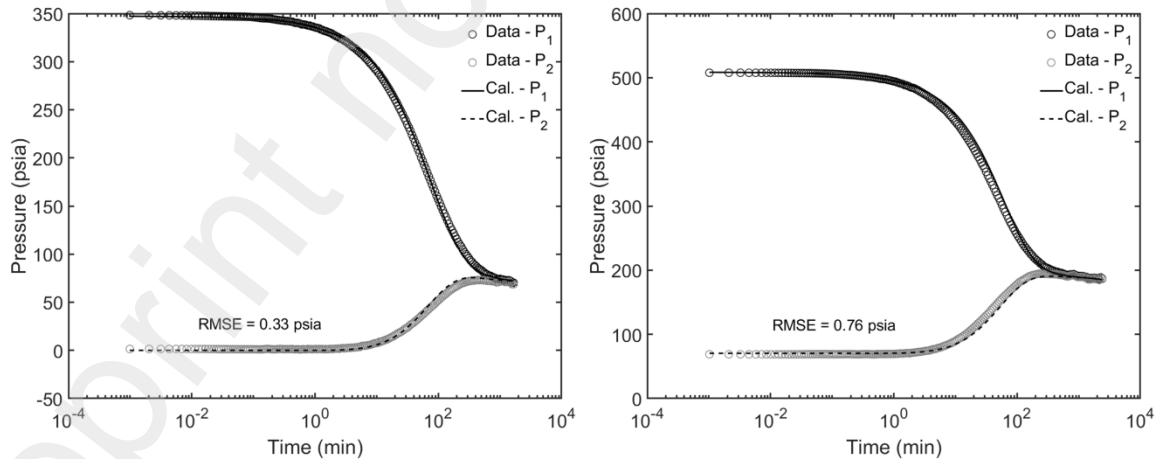


Fig. 12: Comparison of data and calculations for the 1st (left - fitted) and 2nd (right - predicted) CO₂ pressure-decay experiment.

The revised model was then used to predict the behavior of the 2nd CO₂ pulse, and we observe a good agreement (see **Fig. 12** - right). In the revised model, the impact of sorption, porosity reduction (more than 20% in the fracture) and related permeability reduction for the fracture are amplified due to the larger adsorbate volumes (see Appendix F - Fig. F.3). We note that, while a continuous density model is reasonable, variations in the adsorbate density with pressure require further investigation, in particular, for CO₂ adsorption on shale.

4. Summary and Conclusions

In this work, we have studied mass transfer and storage in a core from the Eagle Ford shale with He, Kr, and CO₂. Pressure-pulse decay measurements were utilized to study sample porosity, fracture permeability, mass transfer, and sorption in the matrix. The excess adsorption isotherms for Kr and CO₂ were evaluated based on the average porosity of the shale core, extracted from He pulse-decay measurements, with He considered a nonsorbing gas. The excess isotherms were then interpreted and translated to absolute adsorption by an assumed density model (density of liquid at normal boiling point) using the Langmuir adsorption model for Kr and the BET model for CO₂, respectively.

An effective fracture system, representing 1% of the total pore volume, was utilized to characterize natural fractures or cracks as the main flow conduits in the core. Gas transport in the fracture system was characterized by an apparent permeability k_f , cross-sectional area A_f , and length L_f of the fracture. The apparent permeability was expanded to represent viscous flow (BA_f/L_f) and Knudsen diffusion ($D_k A_f/L_f$) according to the Dusty-Gas-Model (DGM).

A modified analytical approach was introduced, using the later-time data from two pulses of nonsorbing gas, He (e.g., the 1st and 2nd pulses), to estimate the product of the reciprocal of the characteristic time for mass transfer ($\sigma_m D_m$) in the mesopores, and the pore volume of the mesopores relative to up- and down-stream volumes, $V_m(1/V_1 + 1/V_2)$.

We then applied a triple-porosity model (TPM) to estimate the effective permeability of the effective fracture system, the mass transfer rate for the micropores, and the mesopore volume, by matching two He decay experiments simultaneously. The estimated parameters were demonstrated to allow for accurate prediction of a 3rd He decay experiment, to validate the characterization of the gas transport properties and their representation for the shale core.

Excess sorption isotherms were extracted from Kr and CO₂ pulse-decay measurements and converted to absolute sorption using the Langmuir model for Kr and the BET model for CO₂, respectively. The conversion from excess to absolute sorption was performed based on an adsorbate density model (normal boiling point density of liquid).

Transport parameters extracted from He decay experiments were then translated and combined with the isotherm model to predict the behaviors of Kr in the shale core. We demonstrate that the workflow allows for accurate prediction of the Kr pulse-decay experiments with no additional need for parameters estimation. We note that Kr has a moderate affinity to the shale core relative to that of CO₂ and that the representation of porosity variation due to the adsorbate phase has only a marginal impact on the model predictions.

A similar approach was demonstrated to provide a reasonable agreement between modeling/prediction and experimental observations during CO₂ pulse-decay measurements. A central difference between Kr and CO₂ behaviors is attributed to the stronger sorption affinity of CO₂ relative to that of Kr, as observed from the excess data. Model predictions overestimates the apparent permeability of the fracture system due to sorption induced porosity (and permeability) reduction. The observed reduction in apparent permeability can be caused by matrix swelling (strain), in response to adsorption in the shale matrix, or by a build-up of the adsorbate phase in the fracture system. The latter explanation was investigated by applying an alternate representation of the adsorbate density that results in a larger porosity reduction due to adsorption. The alternate density model includes an additional parameter that must be estimated by matching the excess isotherm and one pulse-decay measurement simultaneously. We demonstrate that the modified model predicts a second CO₂ pulse-decay experiment accurately but note that sorption induced strain versus sorption induced porosity reduction cannot be separated based on the experimental data presented in this work.

In summary, we have demonstrated that the analytical approach for interpretation of pulse-decay measurements with He can be modified and used as an efficient tool to delineate the transport coefficients in the shale matrix. Furthermore, we demonstrate that the mass transfer rates can be used in a TPM to interpret efficiently and predict pulse-behavior of He and sorbing gases (Kr and CO₂): The TPM approach provides a practical approach for modeling of shale cores with natural fractures or cracks without the need for a comprehensive discretization of the shale matrix. Application of sorption isotherms provides for reasonably accurate interpretation of gas transport and sorption in shale at low pressure and temperature conditions the gases studies in this work (Kr and CO₂). Furthermore, we demonstrate that the density of the adsorbed phase, for a strongly sorbing gas - CO₂, can have a notable impact on mass transfer and storage behaviors in shale.

Finally, based on the results and analysis presented here, we provide a few recommendations for future work including: 1) Direct measurements of sorption kinetics and isotherms for CO₂ in shale core samples, via e.g. thermogravimetric analysis (TGA), can be instrumental in validating density models for CO₂ adsorption, particularly at higher pressures; 2) Development of experimental techniques for separating the impact of

adsorbate density and matrix swelling during pulse-decay measurements are much needed to provide for a more complete interpretation of experimental observations; 3) The role of surface diffusion was largely ignored in this work and lumped into the characteristic time for mass transfer in the microporous portion of the matrix. Experimental techniques for studying the role of surface diffusion in complex porous materials, including shales, at relevant conditions would allow for a more detailed characterization of combined transport and sorption in this important class of materials.

Acknowledgement

This work was supported as part of the Center for Mechanistic Control of Unconventional Formations (CMC-UF), an Energy Frontier Research Center funded by the U.S. Department of Energy, Office of Science under DOE (BES) Award DE-SC0019165.

Credit author statement

Lyu, Y: Modeling, data interpretation, and manuscript preparation. **Elkady, Y:** Experimental design, experiments, and data interpretation. **Kovscek, A. R.:** Experimental design, data interpretation, manuscript preparation, and funding acquisition. **Jessen, K:** Modeling, data interpretation, manuscript preparation, and funding acquisition. All authors have read and agreed to the published version of the manuscript.

References

Akkutlu, I.Y., Efendiev, Y., Vasilyeva, M., Wang, Y., 2018. Multiscale model reduction for shale gas transport in poroelastic fractured media. *J. Comput. Phys.* 353, 356–376. <https://doi.org/10.1016/j.jcp.2017.10.023>.

Aljamaan, H. C. M. Ross, and A. R. Kovscek, 2017. Multiscale Imaging of Gas Adsorption in Shales. *Society of Petroleum Engineers Journal*, 22(6), 1760-1777. <https://doi.org/10.2118/185054-PA>

Aljamaan, H., R. Holmes, V. Vishal, R. Haghpanah, J. Wilcox, and A. R. Kovscek, 2017b. CO₂ Storage and Flow Capacity Measurements on Idealized Shales from Dynamic Breakthrough Experiments,” *Energy & Fuels*, 31(2), 1193-1207. DOI: 10.1021/acs.energyfuels.6b02286

Alnoaimi, K.R., Kovscek, A.R., 2019. Influence of microcracks on flow and storage capacities of gas shales at core scale. *Transport Porous Media* 127 (1), 53–84. <https://doi.org/10.1007/s11242-018-1180-5>

Amaefule, J. O., Wolfe, K., Walls, J. D., Ajufo, A. O., Peterson, E., 1986. Laboratory determination of effective liquid permeability in low-quality reservoir rocks by the pulse decay technique. Society of Petroleum Engineers. doi: doi:10.2118/15149-MS.

André, M., Malmström M. E., Neretnieks, I., 2009. Specific surface area determinations on intact drillcores and evaluation of extrapolation methods for rock matrix surfaces. *J Contam Hydrol.* 2009 Nov 3;110(1-2):1-8. doi: 10.1016/j.jconhyd.2009.05.003.

Beskok, A., Karniadakis, G., 1999. Report: a model for flows in channels, pipes, and ducts at micro and nano scales. *Microscale Therm Eng* 3, 43–77, DOI: 10.1080/108939599199864.

Brace, W. F., Walsh, J. B., Frangos, W. T., 1968. Permeability of granite under high pressure. *Journal of Geophysical Research (1896-1977)*, 73(6):2225–2236.

Brunauer, S., Emmett, P. H., Teller, E., 1938. Adsorption of gases in multimolecular layers. *Journal of the American Chemical Society*, 60(2):309–319. doi: 10.1021/ja01269a023.

Chalmers, G. R.L., Bustin. R. M., 2008. Lower Cretaceous gas shales in northeastern British Columbia, Part I: geological controls on methane sorption capacity. *Bulletin of Canadian Petroleum Geology*, 56(1):1–21, 03. ISSN 0007-4802. doi: 10.2113/gscpgbull.56.1.1.

Chen, M, Kang, Y, Zhang, T, Li, X, Lin, C., 2019. Shale gas transport behavior considering dynamic changes in effective flow channels. *Energy Sci Eng*; 7: 2059– 2076. <https://doi.org/10.1002/ese3.411>.

Civan, F., 2010. Effective correlation of apparent gas permeability in tight porous media. *Transp. Porous Media* 82, 375–384.

Cui, X., Bustin, A. M. M., Bustin, R. M., 2009. Measurements of gas permeability and diffusivity of tight reservoir rocks: different approaches and their applications. *Geofluids*, 9(3), 208-223.

Dicker, A. I., Smits, R. M., 1988. A practical approach for determining permeability from laboratory pressure-pulse decay measurements. Society of Petroleum Engineers. doi: doi:10.2118/17578-MS.

Energy Information Administration (EIA), 2021. Annual energy outlook 2020 with projections to 2050. U.S. Energy Information Administration Office of Energy Analysis and U.S. Department of Energy.

Elkady, Y., 2020. Multiscale Investigation of Fluid Transport and Enhanced Recovery in Shale (Doctoral dissertation). Stanford University.

Elkady, Y., Kovscek, A. R., 2020a. Multiscale study of the impact of CO₂ on fluid transport and carbonate dissolution in Utica and Eagle Ford shale. *Petroleum Science and Engineering. J. Petrol. Sci. Eng.*, 107867.

Elkady, Y., Kovscek, A. R., 2020b. "Laboratory Visualization of Enhanced Gas Recovery in Shale." Paper presented at the SPE Annual Technical Conference and Exhibition, Virtual, October. doi: <https://doi.org/10.2118/201707-MS>

Elkady, Y., Lyu, Y., Jessen, K., Kovscek, AR., 2020. Three-Dimensional Imaging and Quantification of Gas Storativity in Nanoporous Media via X-rays Computed Tomography. *Energies*; 13(23):6199. <https://doi.org/10.3390/en13236199>.

Freeman, C., Moridis, G., Blasingame, T., 2011. A numerical study of microscale flow behavior in tight gas and shale gas reservoir systems. *Transp. Porous Media* 90, 253–268.

Ghanizadeh, A., Gasparik, M., Amann-Hildenbrand, A., Gensterblum, Y., & Krooss, B. M., 2014. Experimental study of fluid transport processes in the matrix system of the European organic-rich shales: I. Scandinavian Alum Shale. *Marine and Petroleum Geology*, 51, 79-99.

Gupta, D. V. S., 2009. Unconventional fracturing fluids for tight gas reservoirs. Society of Petroleum Engineers.

Heller, R., Vermylen, J., Zoback, M., 2014. Experimental Investigation of Matrix Permeability of Gas Shales, *AAPG Bull.*, 98 (5), 975–995.

Ho, C. K., Webb, S. W., 2006. Gas transport in porous media. (Springer, Dordrecht, the Netherlands).

Javadpour, F., 2009. Nanopores and Apparent Permeability of Gas Flow in Mudrocks (Shales and Siltstone). *Journal of Canadian Petroleum Technology*, 48(08), 16–21. doi: 10.2118/09-08-16-DA.

Kamali-Asl, A., Kovscek, A. R., Zoback, M. D., 2022. Long-term permeability evolution of shale seal rocks with argon and scCO₂, *Journal of Natural Gas Science and Engineering*, Volume 104, 104642, ISSN 1875-5100, <https://doi.org/10.1016/j.jngse.2022.104642>.

Lemmon, E.W., McLinden, M.O., Friend, D.G., 2005. In: Thermophysical Properties of Fluid Systems. NIST Chemistry Webbook, vol. 69. NIST standard reference database.

Li, C., Carman, P. S., Davis, B. J., 2018. Modern fracturing revitalizes dormant technologies: A case history. Society of Petroleum Engineers.

Lim, K., Aziz, K., 1995. Matrix-fracture transfer shape factors for dual-porosity simulators. *J. Petrol. Sci. Eng.* 13 (3–4), 169–178. [https://doi.org/10.1016/09204105\(95\)00010-F](https://doi.org/10.1016/09204105(95)00010-F).

Lin, W., Kovscek, A. R., 2014. Gas sorption and the consequent volumetric and permeability change of coal I: Experimental. *Transport in Porous Media*, 105:371 – 389. ISSN 1573-1634. doi: 10.1007/s11242-014-0373-9.

Lu, X.C., Pepin, G.P., Moss, R.M., Watson, A.T.. "Determination of Gas Storage in Devonian Shales With X-Ray-Computed Tomography." Paper presented at the SPE Annual Technical Conference and Exhibition, Washington, D.C., October 1992. doi: <https://doi.org/10.2118/24810-MS>

Lyu, Y., Dasani, D., Tsotsis, T., Jessen, K., 2021. Characterization of shale using Helium and Argon at high pressures, *Journal of Petroleum Science and Engineering*, doi: <https://doi.org/10.1016/j.petrol.2021.108952>

Lyu, Y., Dasani, D., Tsotsis, T., Jessen, K., 2022. Investigation of Methane Mass Transfer and Sorption in Marcellus Shale Under Variable Net Stress. *Journal of Petroleum Science and Engineering*, submitted for review.

Mason, E.A., Malinauskas, A.P., 1983. *Gas Transport in Porous Media: The Dusty-gas Model*, Elsevier Science Ltd., New York.

Nuttall, B. C., Eble, C. F., Drahovzal, J. A. D., Bustin, R. M., 2005. Analysis of Devonian Black Shales in Kentucky for Potential Carbon Dioxide Sequestration and Enhanced Natural Gas Production. doi: 10.2172/920185.

Peng, S., Ren, B., and Meng M., 2019. "Quantifying the Influence of Fractures for More-Accurate Laboratory Measurement of Shale Matrix Permeability Using a Modified Gas-Expansion Method." *SPE Res Eval & Eng* 22: 1293–1304. doi: <https://doi.org/10.2118/195570-PA>

Roy, S., Raju, R., Chuang, H.F., Cruden, B.A., and Meyyappan, M. 2003. Modeling gas flow through microchannels and nanopores. *Journal of Applied Physics*, 93(8), pp. 4870–4879.

Sakhaee-Pour, A., Bryant, S. L., 2012. Gas permeability of shale. *SPE Reserv Eval Eng* 15, 401–409, DOI: 10.2118/146944-PA.

Schaaf, S.A. and Chambre, P.L. 1961. *Flow of Rarefied Gases*. Princeton University Press, Princeton, NJ.

Sinal, M. L., Lancaster, G., 1987. Liquid CO fracturing: Advantages and limitations. *Petroleum Society of Canada*.

Vermeulen, T., 1953. Theory for Irreversible and Constant-Pattern Solid Diffusion. *Industrial & Engineering Chemistry*, 45(8), 1664–1670. doi: 10.1021/ie50524a025.

Vega, B., Dutta, A., Kovscek, A. R., 2014. CT imaging of low-permeability, dual-porosity systems using high X-ray contrast gas. *Transport in Porous Media*, 101(1):81–97. ISSN 1573-1634. doi: 10.1007/s11242-013-0232-0.

Wasaki, A., Akkutlu, I.Y., 2015. Permeability of organic-rich shale. *SPE J.* 20 (6) <https://doi.org/10.2118/170830-MS>, 1,384-1,396.

Wu, W., Sharma, M. M., 2017. Acid fracturing in shales: Effect of dilute acid on properties and pore structure of shale. Society of Petroleum Engineers. doi: 10.2118/173390-PA.

Yamada, S. E. Jones, A. H., 1980. A review of a pulse technique for permeability measurements.

Zhang, J., Raslan, M., Wu, C., Jessen, K., "A Generalized Dynamic Transfer Function for Ultra-Tight Dual-Porosity Systems." Paper presented at the SPE Western Regional Meeting, Bakersfield, California, USA, April 2022. doi: <https://doi.org/10.2118/209324-MS>

Zimmerman, R. W., Chen, G., Hadgu, T., Bodvarsson, G. S., 1993. A numerical dual-porosity model with semianalytical treatment of fracture/matrix flow. *Water Resources Research*, 29(7), 2127–2137. doi: 10.1029/93wr00749

Appendix A – Sensitivity of V_f on pulse decay

In this sensitivity analysis, only the volume of the effective fracture was altered (0.1% to 10% of V_f) in the triple-porosity model (TPM) with other parameters manually assigned and fixed. The calculation results demonstrate the modest impact of the fracture volume on the pressure decay in the core.

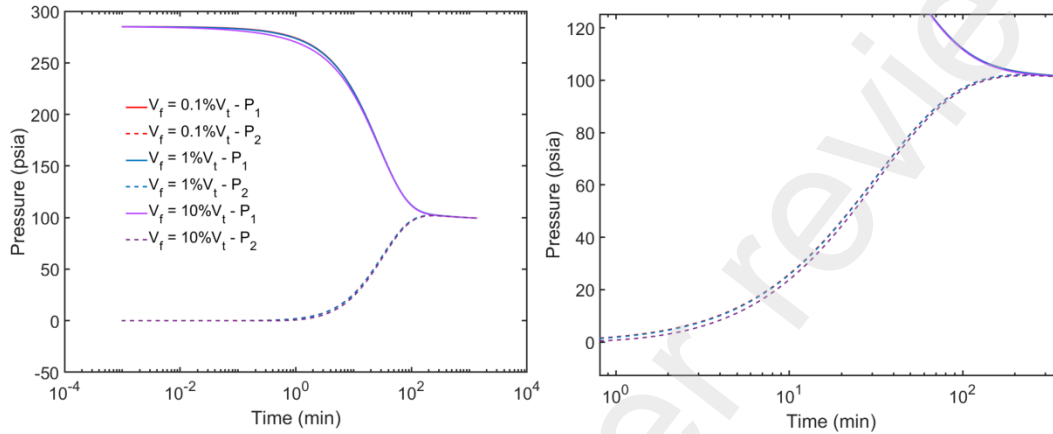


Fig. A.1. Sensitivity test for the fracture volume on modeling results for the 1st pulse of He pressure decay using TPM (original on the left, close-up view on the right)

Appendix B – Classification of flow regime from Knudsen number

The flow regime can be classified and determined based on the Knudsen number (Schaaf and Chambre, 1961; Roy et al., 2003): Viscous flow ($Kn \leq 0.001$), slip flow ($0.001 < Kn < 0.1$), transition flow ($0.1 < Kn < 10$), Knudsen flow ($Kn \geq 10$). Subject to the gases involved and relevant temperature and pressure conditions in this work, the Knudsen number can be evaluated for gas transport through different sizes of cylindrical pores.

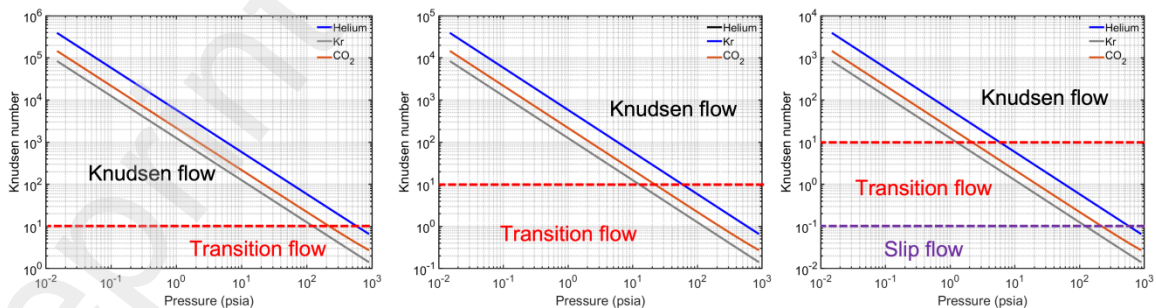


Fig. B.1. Flow regime classification based on Knudsen number for different pore diameters (1 nm - left, 10 nm - middle, 100 nm - right) at relevant conditions of this work

Appendix C – Representation of effective diffusivity in mesopores

Beskok and Karniadakis (1999) developed a second-order correction to the apparent permeability (k_a) based on the Knudsen number due to gas slippage in tight porous media:

$$k_a = k_i f_c, f_c = (1 + \alpha(Kn)Kn) \left[1 + \frac{4Kn}{1 - bKn} \right], \quad (B-1)$$

where k_i is the intrinsic permeability, b is the slip coefficient ($b = -1$ for slip flow), $\alpha(Kn)$ is the rarefaction coefficient, as discussed by Civan (2010):

$$\alpha(Kn) = \frac{1.358}{1 + 0.170Kn^{-0.4348}}. \quad (B-2)$$

We note that some contributions, including Beskok and Karniadakis (1999) use the hydraulic radius to calculate the Knudsen number, rather than the hydraulic diameter. Then the effective diffusivity can be computed as:

$$D_m = \frac{p}{\mu} \left(1 + \frac{C}{z} \frac{dz}{dC} \right) \cdot k_a \quad (B-3)$$

where μ (psia·s) is the gas viscosity, k_a and k_{int} (cm²) are the apparent and the intrinsic permeability, respectively. C (mol/cm³) is the gas concentration and z is the gas compressibility factor. f_c is the BKC correction factor.

The effective diffusivity in tight porous media can also be described by the DGM (Mason and Malinauskas, 1983), which combines viscous flow and Knudsen diffusion in the total flux:

$$D_m = \frac{p}{\mu} B \left(1 + \frac{C}{z} \frac{dz}{dC} \right) + D_k, \quad (B-4)$$

where B (cm²) is the viscous flow parameter and D_k (cm²/s) is the Knudsen diffusion coefficient. For a cylindrical pore with radius r_p , B and D_k can be evaluated from

$$B = \frac{r_p^2}{8}, D_k = \frac{2r_p}{3} \sqrt{\frac{8RT}{\pi M_w}}. \quad (B-5)$$

R (J/mol/K) is the gas constant, T (K) is the temperature, and M_w (kg/mol) is the molecular weight.

A comparison of the two models, in terms of the effective diffusivity through capillary tubes, is reported below. Although the effective diffusivity could differ by as much as 25% (He in a small diameter tube), the ratio used to rescale the diffusivity between different gases is relatively close (about 7% as a maximum).

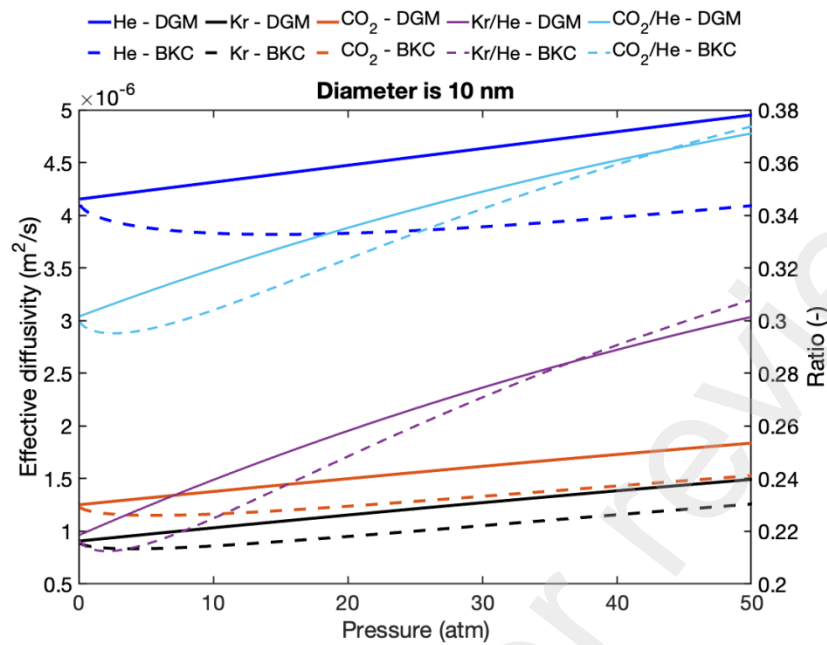


Fig. C.1. Effective diffusivity and their ratios among gases determined by DGM and Beskok-Karniadakis-Civan (BKC) in a 10 nm cylindrical pore

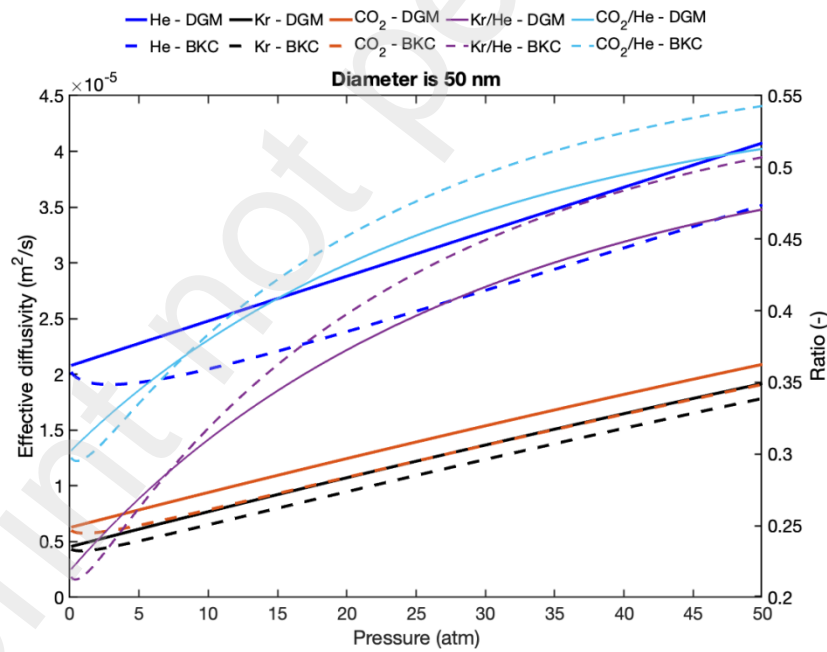


Fig. C.2. Effective diffusivity and their ratios among gases determined by DGM and BKC in a 50 nm cylindrical pore

Appendix D – Workflow for estimating model parameters

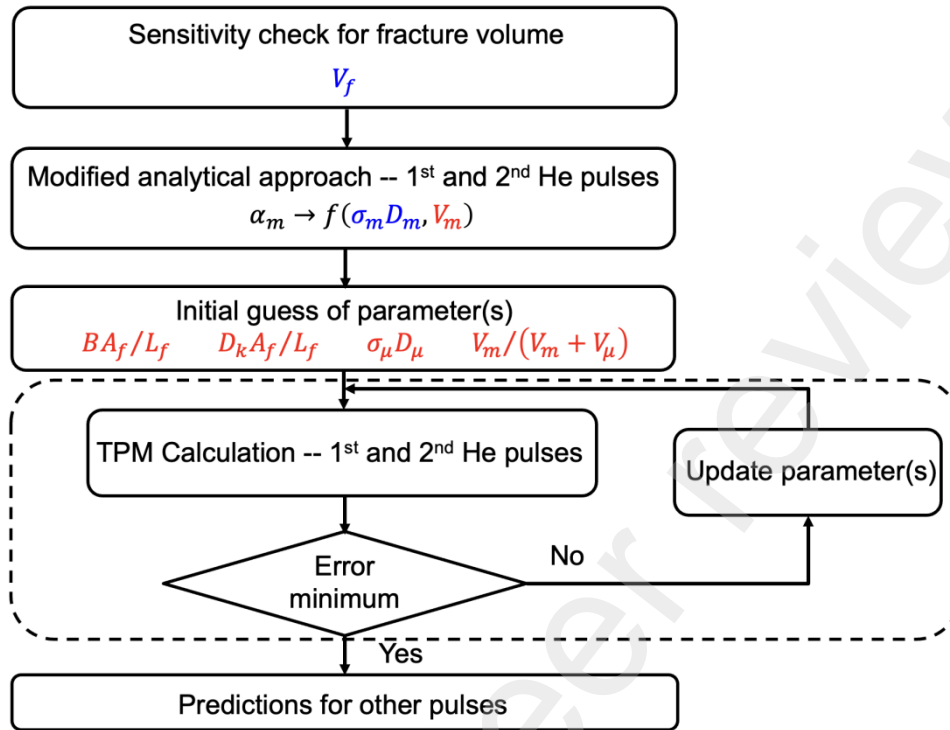


Fig. D.1. Workflow summary of this work

Appendix E – Revised density model and BET isotherm

Excess adsorption isotherms of CO₂ as evaluated from the BET model with the revised adsorbate density model.

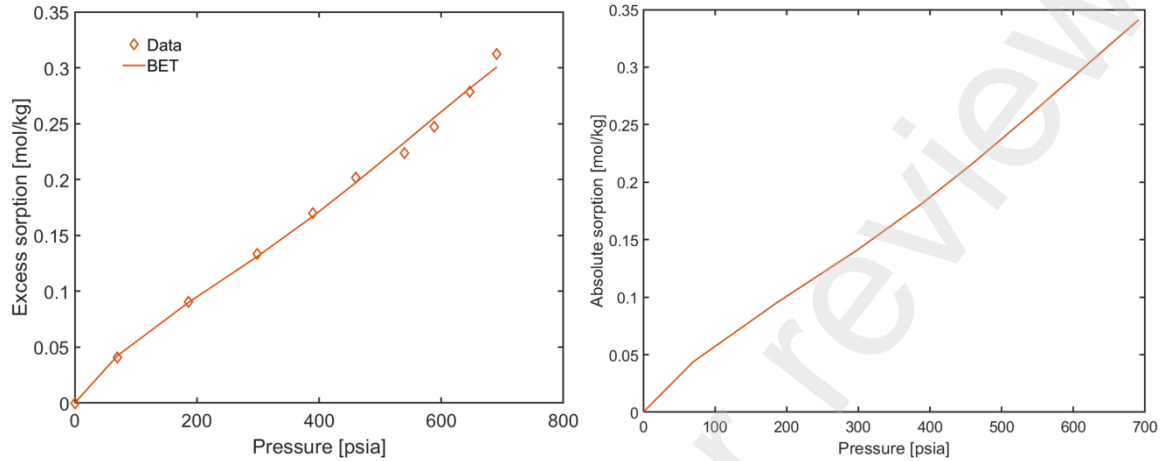


Fig. E.1. Excess adsorption (left) and absolute adsorption (right) modeling results.

Table E.1: Model parameters for CO₂ adsorption isotherms with revised density model

ρ_{ads} (mol/cm ³)	$C_{s,max}$ (mol/kg)	c (-)	n (-)
$12.26e-3 \cdot \theta^{2/3}$	121.57e-3	5.39	6

Appendix F – Porosity reduction due to gas adsorption

Calculated porosity reductions for sorbing gases, Kr and CO₂, are reported below:

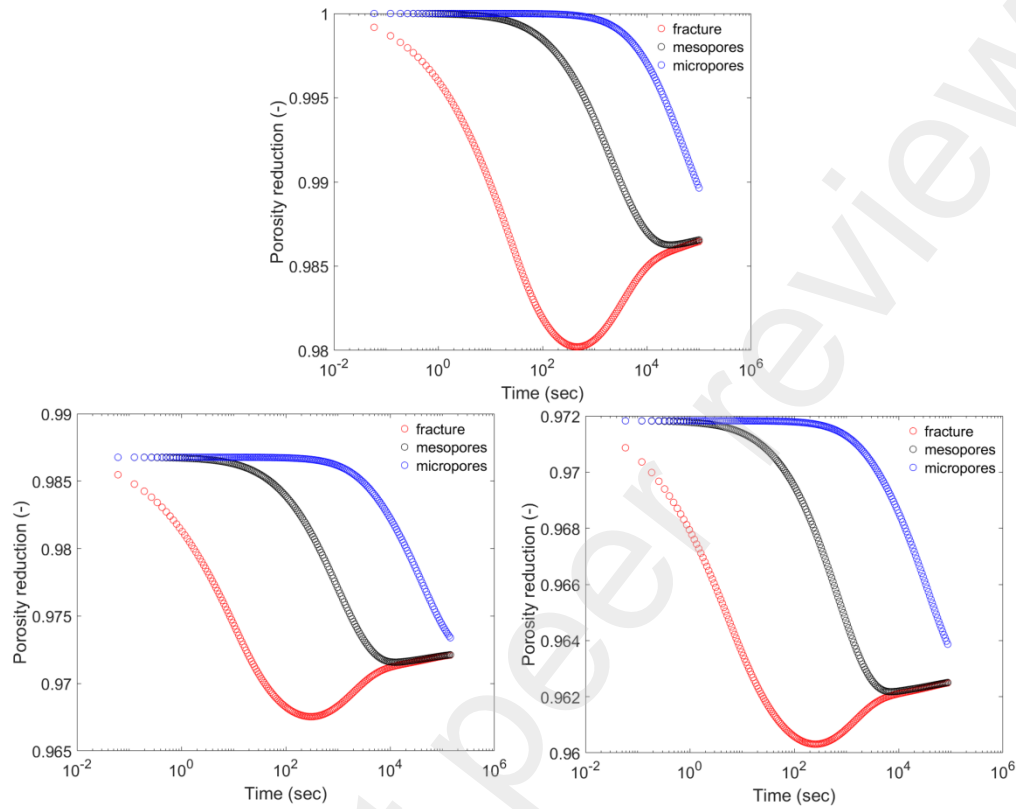


Fig. F.1. The porosity reduction for pressure-pulse decays of Kr (1st pulse – top, 2nd pulse – bottom left, 3rd pulse - bottom right)

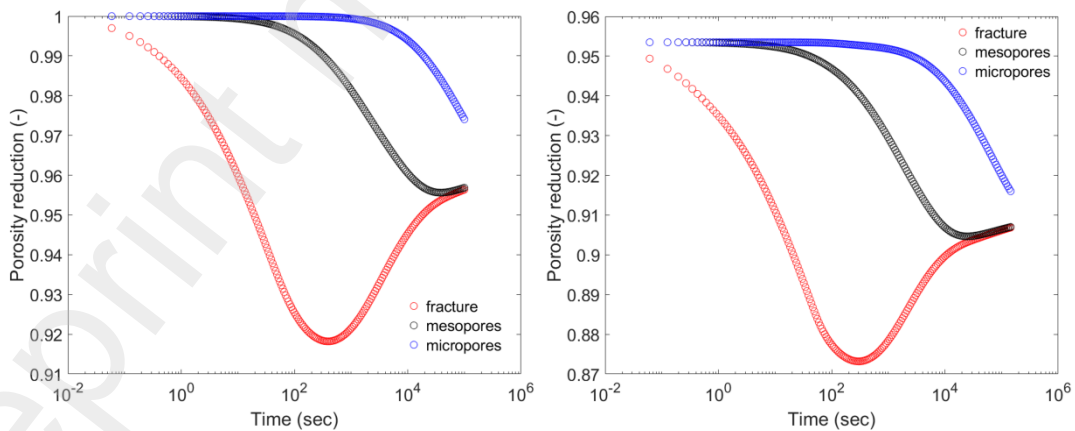


Fig. F.2. The porosity reduction for pressure-pulse decays of CO₂ (1st pulse – left, 2nd pulse - right) with $\rho_{ads} = 1.10 \text{ g/cm}^3$

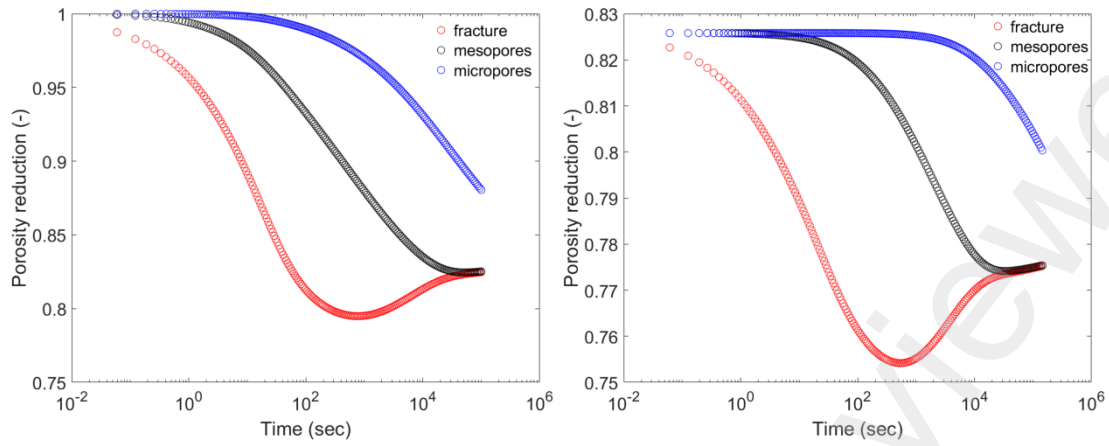


Fig. F.3. The porosity reduction for pressure-pulse decays of CO₂, the 1st pulse (left) and the 2nd pulse (right) with $\rho_{ads} = 12.26e-3 \cdot \theta^{2/3}$ mol/cm³